Princeton Plasma Physics Laboratory

PPPL- 5096

PPPL-5096

Correlations between Quasi-coherent Fluctuations and the Pedestal Evolution during the Inter-ELM Phase on DIII-D

A. Diallo, R.J. Groebner, T.L. Rhodes, D.J. Battaglia,
D.R. Smith, T.H. Osborne, J.M. Canik,
W. Guttenfelder, and P.B. Snyder

December 2014

PPPL PRINCETON PLASMA PHYSICS LABORATORY

Prepared for the U.S. Department of Energy under Contract DE-AC02-09CH11466.

Princeton Plasma Physics Laboratory
Report Disclaimers

Full Legal Disclaimer

Trademark Disclaimer

PPPL Report Availability

Princeton Plasma Physics Laboratory:

http://www.pppl.gov/techreports.cfm

Office of Scientific and Technical Information (OSTI):

http://www.osti.gov/scitech/

Related Links:

U.S. Department of Energy

Office of Scientific and Technical Information

Correlations between quasi-coherent fluctuations and the pedestal evolution during the inter-ELM phase on DIII-D

A. Diallo,[1] R.J. Groebner,[2] T.L. Rhodes,[3] D.J. Battaglia,[1] D.R. Smith,[4]
T.H. Osborne,[2] J.M. Canik,[5] W. Guttenfelder,[1] and P.B. Snyder[2]

[1]*Princeton Plasma Physics Laboratory,*
P.O. Box 451, Princeton, NJ 08543-0451, USA
[2]*General Atomics, P.O. Box 85608, San Diego, CA 92186-5608, USA*
[3]*University of California Los Angeles,*
P.O. Box 957099, Los Angeles, CA 90095-7099, USA
[4]*University of Wisconsin-Madison, 1500 Engineering Dr., Madison, WI 53706, USA*
[5]*Oak Ridge National Laboratory, P.O. Box 2008, Oak Ridge, TN 37831, USA*

(Dated: December 4, 2014)

Abstract

Direct measurements of the pedestal recovery during an edge-localized mode cycle provide evidence that quasi-coherent fluctuations (QCFs) play a role in the inter-ELM pedestal dynamics. Using fast Thomson scattering measurements, the pedestal density and temperature evolutions are probed on sub-millisecond time scales to show a fast recovery of the density gradient compared to the temperature gradient. The temperature gradient appears to provide a drive for the onset of quasi-coherent fluctuations (as measured with the magnetic probe and the density diagnostics) localized in the pedestal. The amplitude evolution of these QCFs tracks the temperature gradient evolution including its saturation. Such correlation suggests that these QCFs play a key role in limiting the pedestal temperature gradient. The saturation of the QCFs coincides with the pressure gradient reaching the kinetic-balloooning mode (KBM) critical gradient as predicted by EPED1. Furthermore, linear microinstability analysis using GS2 indicates that the steep gradient is near the KBM threshold. Finally, the modeling supports the observations and together suggest that QCFs may be KBMs.

I. INTRODUCTION

With the discovery of the H-Mode [1], significant research has been undertaken to understand the formation of the edge pressure pedestal. The pedestal pressure can be considered as a boundary condition for the core and theoretical modeling predicts that the pedestal height has a strong influence on core fusion power [2]. Hence, an understanding of the pressure pedestal height and width formation is important for the predictive capability of future fusion devices.

The maximum achievable pedestal parameters have been commonly observed to be limited by edge instabilities known as edge localized modes (ELMs). While the high heat and particle fluxes of ELMs pose a threat for the plasma-facing components' lifetime on future devices such as ITER, the pedestal height leading up to an ELM is much desired for optimum core performance. An understanding of the dynamic of the pedestal parameters leading up to an ELM is far from complete. As a result, research efforts have been intensified with the objective to probe the pedestal recovery for a better formulation of the physical mechanism in the pedestal formation.

At present, the leading pedestal predictive model is EPED1, which was successful in predicting the pedestal pressure height and width at the ELM *onset* on multiple devices [3, 4]. EPED1 is based in two main hypothesis, namely, peeling-ballooning macro-instability which triggers an ELM, and kinetic ballooning mode (KBM) which limits the pressure gradient prior to the onset of the ELMs. While the crossing of the peeling-ballooning boundary is widely accepted as the trigger for ELMs, definitive evidence of KBM providing a saturation mechanism for the pedestal has yet to be demonstrated. Multiple machines show that edge pressure gradient establishes fairly rapidly in the recovery phase after an ELM [5–7]. In addition, AUG determined that the density gradient recovers faster than the temperature gradient for various fueling rates [8]. Once the gradient recovers, the pedestal pressure proceeds to expand at constant gradient until the next ELM [5, 9]. Previous experiments on DIII-D have also shown that the pedestal pressure gradient tracks approximately the predicted KBM critical gradient prior to the ELM crash [10]. To improve our understanding of KBM regulating transport, experiments have been executed with the objective to resolve the pedestal gradient recovery on a fast time scale together with characterizing edge fluctuations associated with the pedestal dynamics.

Here, we focus on both the pedestal electron density and temperature recovery after an ELM crash for various plasma currents and the associated edge fluctuations. This work represents the first detailed profile response analysis after an ELM crash as a function of plasma current with the associated fluctuations correlated with the pedestal parameter dynamics. The results clearly show that the pedestal density gradient recovers on a 3-5 ms time scale for various plasma currents. The pedestal temperature gradient recovery, on the other hand, takes between 5 and 15 ms for the range of plasma currents investigated. Using the edge density fluctuation diagnostics, we observed onset of the quasi-coherent fluctuations (QCFs) when the temperature gradient reaches a threshold. Subsequently, the QCF correlates and tracks the temperature gradient evolution including its saturation until the next ELM.

These QCFs are found to be localized in the pedestal region and have magnetic signatures. These observations are consistent with the edge dynamic picture suggesting that the edge temperature gradient provides the necessary free energy to drive these quasi-coherent fluctuations, which in turn limit the pedestal parameters. These quasi-coherent fluctuations are reminiscent of those observed in other H-mode regimes [11–13] (e.g., edge-harmonics oscillations in quiescent H-modes (QH), quasi-coherent modes in enhanced D_α H-mode (EDA), and the weakly-coherent mode in I-mode). The quasi-coherent mode (QCM) in C-Mod was recently observed to be localized in the lower part of the steep gradient region and to regulate both particle and density transport [14]. During the inter-ELM phase, however, the quasi-coherent fluctuations appear to be localized in the pedestal region and most importantly to track the pedestal temperature gradient dynamics. Applications of EPED1 to the pedestal dynamics show that the pressure gradient reaches the KBM critical gradient. In addition, a linear local microinstability analysis using GS2 indicates that the steep gradient is near the KBM threshold.

This paper presents the detailed profile evolutions made possible using the burst Thomson scattering systems in the following section. Section III describes the measurements of the inter-ELM fluctuations and provides characterization of the quasi-coherent fluctuations. Section IV correlates QCFs with the pedestal parameters dynamics. Comparisons of the edge parameter dynamics using the EPED1 framework are provided in Sec. V followed by an initial microinstabiility analysis using GS2. Finally, a summary and discussions are provided.

II. PEDESTAL PARAMETERS DYNAMICS

The experiments were carried out on the DIII-D tokamak at fixed $B_T = 1.9\,T$ for three plasma currents (0.7 MA, 1 MA, 1.6 MA). These type I ELM discharges were run in a lower single null configuration with the ion $B\times\nabla B$ drift direction toward the X-point. Time histories of low and high plasma current cases are displayed in Fig. 1. These experiments were targeted at capturing the pedestal recovery after an ELM crash using the recently upgraded Thomson scattering system [15]. To accurately resolve the inter-ELM dynamics, the lasers were fired in a bunch mode, which enabled temporal resolution of up to 100 μs. This increase in temporal resolution is achieved by adding more lasers to the same path with pulses interleaved in time. Normally, the lasers are phased to produce pulses at fairly regular intervals (exact regularity is not possible with the specific combination of 20 Hz and 50 Hz lasers being used). In bunch mode, the phase shifts are adjusted so that all lasers fire in rapid succession, followed by a cool down. The spatial resolution in the edge was sufficient to provide modified-tanh fits for each time slice. An example of the quality of the data is shown in Fig. 2, where the profile dynamics for the electron density and temperature are displayed.

Pedestal parameters, such as width and height, are obtained by fitting analytic functions to each time slice. These functions incorporate a tanh function to model the steep gradient region in the pedestal. The tanh function is smoothly joined to polynomial or spline functions to provide accurate fits to the profiles as they extend into the core and into the scrape-off layer (SOL) [16]. Figures 3 and 4 show the pedestal parameters (e.g., height and width) relative to the time after an ELM crash for the low and high current cases. It is evident from these figures that each ELM causes a prompt drop of the pedestal heights during which the widths expand. These width expansions vary from low to high current [Figs 3(b,d) and 4(b,d)], indicating that at high plasma currents the ELMs have a deeper radial perturbation than at low current. Such deeper radial perturbation, although beneficial for impurity flushing as shown in Fig. 4 of Ref. [17], suggests that the rebuild of the pedestal takes a longer time because more heat will be required to thermalize the colder particles fueling the pedestal. Finally, for completeness, the evolution of the radial electric field is obtained and displayed in Fig. 5. The dynamics of the radial electric field are key players for generating the transport barrier and consequently the pedestal observed in high confinement regimes. From Fig. 5,

it is clearly seen that the radial electric field recovery time increases from ~ 6 ms to ~ 10 ms as I_p increases, which is consistent with the pressure gradient recovery (shown in Fig. 8). Below, we refer to pedestal recovery time as the time it takes for the pedestal parameters to reach their saturated values prior to the ELM onset.

The variation of pedestal recovery time is clearly evidenced when the pedestal gradients are computed as shown in Figs 6 and 7. In these figures, the evolution of both density and temperature gradients are displayed. In the low plasma current case (Fig. 6), the recovery time is highlighted for both the temperature and density gradients. Note that the density gradient recovers a little faster than that of the temperature. This difference in gradient recovery time is amplified when the plasma current is increased. For instance, at high currents as shown in Fig. 7, the temperature gradient recovers slowly. While this slow recovery is not yet understood, one can perhaps speculate that such recovery can be attributed to heating of the cold recycled particles. More specifically, once the density recovered, the pedestal contains cold particles and heat from the core is required to thermalize them. At higher current more particles are recycled and require more time to be heated at fixed heat source. In addition to differences in recovery rates, the saturation levels of the density and temperature gradients also increase from low to high I_p case.

The recovery time is documented for three plasma current cases in Fig. 8. Note that the density recovery times appear to be independent of the plasma current. The temperature and the pressure gradients recovery times, on the other hand, increase with plasma current. In addition to the recovery time during intrinsic ELMs, we also probed the recovery time during non-resonant-magnetic-perturbation (RMP)-induced ELMs to improve the odds of capturing the inter-ELM dynamics using the Thomson scattering system in bunch mode. This was achieved by synchronizing the laser bursts with the imposed RMP currents. This RMP-induced ELM pacing approach was demonstrated in Ref. [18] in a wide range of plasma conditions. Here, ELM pacing was utilized to compare intrinsic and RMP-paced ELMs. In both cases the pedestal recovery time scale was similar. We then focused on intrinsic ELMs for the remainder of this paper. With the detailed study of the edge parameters right after an ELM crash until the next ELM, the question arises: What transport mechanism limits the pedestal dynamics?

III. INTER-ELM EDGE FLUCTUATIONS

Dedicated measurements of the edge fluctuations during the pedestal recovery have been performed to further investigate the limiting mechanism of the pedestal parameters. More specifically, the magnetic and density fluctuations are examined. Note that due to the high densities in these discharges, we were unable to obtain electron cyclotron emission (ECE) data at the edge.

Figure 9 shows the magnetic fluctuations using a Mirnov probe located 1 cm behind the boron nitride cover plate. The inter-ELM magnetic fluctuations preceding ELMs are shown in Fig. 9(a,b) for both plasma currents. In these plots, it can be clearly observed that after an ELM crash, there is a gap in the magnetic spectrograms followed by the onset of quasi-coherent fluctuations as indicated by the arrows. In Fig. 9(a), which represents the low current case, the quasi-coherent fluctuations appear on top of broadband fluctuations. In the high current case, on the other hand, two frequency bands are observed near 90 kHz and 120 kHz. Note that in the Fig. 9(b), the low frequency ($\sim$ 50 kHz) has been determined to be a tearing mode or ELM unrelated events (more likely core fluctuations). Overall, there is clear evidence of quasi-coherent fluctuations preceding an ELM. Magnetic mode analysis for the low current case is shown in Fig. 10. Preceding the ELMs, the most dominant mode activities in Fig. 10 are n=-2 and n=-3. Here the negative direction indicates propagation in the ion diamagnetic direction. Since the magnetic probes were sampled at 250 kHz, the high current case mode analysis could not be performed.

Similarly, on Alcator C-Mod, a QCF with electromagnetic signatures has been detected using a double-head probe located 2 cm from the separatrix [19]. On JET, similar quasi-coherent modes were observed as ELM-related events and were called washboard modes [20, 21]. There the modes showed multiple frequency spectra, hence their name "washboard modes". On DIII-D, high frequency coherent (HFC) modes were observed in QH-mode plasmas with some features qualitatively similar to those expected for KBMs [22]. In addition, characteristics of a long poloidal wavelength and low frequency band of fluctuations were observed during ELM recovery. This saturation of these fluctuations is correlated with the electron pressure gradient [23], qualitatevely consistent with KBMs. Finally, previous experiments on DIII-D indicated the onset of coherent modes on the beam emission spectroscopy (BES) diagnostics shortly after L-H transition [10], which appears to slow down

the evolution of the pressure gradient leading up to the first ELM. Moreover, the pressure gradient is shown to be close to the KBM critical gradient.

The natural followup in characterization of this quasi-coherent mode is to provide its radial localization. For the low current case in Fig. 11(a), the BES inter-ELM fluctuation amplitude averaged between 20 and 120 kHz (encompassing the quasi-coherent mode) is displayed indicating radial localization of the fluctuation intensity in the pedestal region and more specifically near the pedestal top instead of the steep gradient. Definite localization, however, in either the pedestal top or the steep gradient region remains uncertain. In fact, these radial positions are determined once the finite beam lifetime and viewing volume spot size effects, and the EFIT mappings uncertainties are included in Fig. 11(b) with points indicating the location of BES points. Note that the EFIT mapping uncertainty (of order 1-2 cm) mostly stems from the fact that the pedestal profiles are maps from data on the Thomson vertical chords to the mid plane radius to enable localization against other diagnostics.

Similarly, in the high current case, as shown in Fig. 12, the QCF is localized in the pedestal region near the pedestal top as shown in Fig. 12(a-c). For guidance, the bottom right panel of Fig. 12 shows the magnetic signatures. Note that here, the QCF appears to be localized in a rather narrow layer in the pedestal region. Overall, this QCF has strong magnetic signatures with weak associated density perturbation, which is localized in the pedestal region within uncertainties.

IV. CORRELATIONS BETWEEN INTER-ELM QUASI-COHERENT MODES AND THE PEDESTAL EVOLUTION

These observations of the QCF on the magnetic and density diagnostics provide the opportunity to test the correlation with the pedestal parameters' evolution. To test any correlation between these QCF and the pedestal parameters, the amplitude of these fluctuations are extracted from the magnetic spectrogram and conditionally-averaged with ELMs being the condition. These are then replotted as a function of time relative to an ELM. Figure 13(a) displays the magnetic spectrogram with the double arrow indicating the region of interest plotted on Fig. 13(b). This figure shows the conditionally-averaged amplitudes' evolutions of the frequency band between 23 kHz through 60 kHz as a function time relative

to an ELM. Correlation of these amplitudes' evolutions with the gradient of the pedestal temperature can readily be assessed. It is clearly seen that the amplitude of the QCF onsets for a given temperature gradient and then monotically increases until saturation is reached. Such saturation coincides with the temperature gradient saturation.

Figure 14(a) displays the temporal evolutions of the pedestal gradient and the scaled amplitude of the QCF between 120 and 170 kHz at the high current case. Note that this frequency band is the only one that correlated with gradient evolution. As can been seen in Fig. 14(a), there is clear onset of the QCF and a temporal evolution including its saturation which again coincides with the saturation of the gradient similar to the low current case. In Fig. 14(b), the amplitude of the QCF is plotted against the gradient to further emphasize the threshold gradient at which the QCF onsets. Overall, the QCF appears to be driven by temperature gradient in both the low current and high current case.

This correlation/coincidence with temperature gradient has also been observed on Alcator C-Mod [19], pointing to a similar physical mechanism at play in both machines during the inter-ELM phase. It is worth noting that similar correlations of the BES broadband fluctuations with the gradients of pressure, density, and temperature have been observed previously on DIII-D in Fig. 10 of Ref. [23]. A simple picture for halting the pedestal evolution is proposed. After an ELM crash, because there is very little local electron heating in the pedestal, electron heat mostly flows radially from the core through the pedestal. This heat contributes to building up the pedestal until a threshold gradient is reached. At that gradient, the onset of quasi-coherent fluctuations localized in the pedestal region provides the necessary transport to limit and saturate the pedestal gradient but allow the the pedestal height and width to possibly increase until the next ELM. Note that a time-dependent calculation between ELMs is needed to test this hypothesis and will be the subject of further work.

Doppler backscattering (DBS) [24, 25] is a diagnostic where a microwave beam is launched at a frequency that approaches a cutoff in the plasma and at an angle that is oblique to that cutoff. This diagnostic enables measurement of the density fluctuations at intermediate scale ($k_\theta \rho_s \sim 1$). For the low current case as shown in Fig. 15, the root-mean-square (rms) density fluctuations as measured using DBS show a drop of the rms level after an ELM crash followed by a quiet period lasting ~ 7 ms. Note that this time corresponds to the QCF amplitude evolution as shown in Fig. 13(b). After this period, the density fluctuations

increase due to either pedestal density or temperature gradient recovery since for this low current case these gradient recovery times are similar. The probing scale corresponds to $k_\theta \rho_s \sim 0.9$ in the steep gradient region ($\psi_n = 0.95 \rightarrow 0.96$). For the high current case (not displayed here), the rms density fluctuations are observed to recover quickly within the same 5-7 ms. The DBS rms fluctuations at $k_\theta \rho_s \sim 0.03$-0.1 are correlated with the density gradient in the steep gradient region.

Using BES poloidally separated views, one can also determine the poloidal correlation length of density fluctuations, which for the low current case yields an e-folding length of $\lambda_\theta \sim$ 5-6 cm, as shown in Fig. 16. In this figure, the poloidal correlation is computed starting from 5.1 ms after an ELM crash when the density gradient is recovered and when there is magnetic quasi-coherent fluctuations activity. The poloidal scale is therefore indicative of the quasi-coherent fluctuation scale. This scale corresponds to $\mathrm{k}_\theta \rho_s \sim 0.1$. The difference between DBS and BES in the estimates of $\mathrm{k}_\theta \rho_s$ stems from the different radial regions probed by each diagnostic and the different wave numbers sensitivities. More specifically, the correlation length measured by BES was obtained for poloidallly separated points shown in Fig. 11(a) corresponding to the pedestal top. The DBS channels probing the pedestal recovery measured fluctuations in the steep gradient $\psi_n = 0.95 \rightarrow 0.96$. In addition, BES correlation analysis yields the dominant turbulent wavenumber. DBS, on the hand, is tuned to only accept wavenumber $k_\theta \rho_s \sim 0.9$ in the steep gradient in this particle case, which might not always corresponds to the dominant wavenumber.

For completeness, BES data analysis in the high current case was performed for the QCF frequency band (120-170 kHz) showing the best correlation with temperature gradient evolution (shown in Fig. 14) to determine the wavenumber. Figure 17 displays high coherency for the frequency band 120-170 kHz, which enables the determination of a poloidal/vertical wavenumber of $\mathrm{k}_\theta \sim 0.18$-0.2 rad/cm propagating in the electron diamagnetic direction in the laboratory frame. This propagation direction is still in the electron direction once the E×B velocity (~ 14 km/s) is taken into account.

In summary for the high current case where the density and temperature gradient recovery are more clearly distinct, we observe that the QCF onsets at a given temperature gradient threshold. The amplitude of QCF tracks well the temperature gradient evolution including when the temperature gradient saturates. These fluctuations are pedestal localized and are of ion scale with $\mathrm{k}_\theta \sim 0.18$-0.2 rad/cm that propagates in the electron diamagnetic direction

in the plasma frame. Assessing the level of transport produced by these low-k fluctuations will require nonlinear gyrokinetic calculations in the edge which will be the subject of future work.

V. EPED1 PREDICTIONS AND MICROINSTABILITY ANALYSIS

This section utilizes the EPED1 framework to study the pressure gradient evolution and compare it to experiment for both the low and high current case. Previous plasma current scans experiments on DIII-D provided tests of the EPED1 predictions and have shown reasonable agreement with measurements during the latter part of the ELM cycle (Fig. 2 of Ref. [26]). In addition, for plasma current of 0.5 MA, it was shown that the total pressure pedestal evolved along the KBM critical gradient (Fig. 5 of Ref. [26]). Below, a similar approach is used to interpret the dynamic ELM cycle for both high and low current using EPED1. Note that EPED1 is a static model, designed to predict the structure of a fully developed pedestal. We used it to determine the pedestal gradient dynamics.

Figure 18 displays the gradient evolution against the time relative to an ELM. In each plot, the red squares indicate the binned averages of experimental data. From each of the data, the EPED1 model requires eight input parameters, (B_T, I_p, R, a, κ, δ, global β, and n_e^{ped}) from which it outputs the pedestal pressure height and width (see Ref. [27] for further details). Here, given that experimental observations give fast measurements of n_e^{ped} and T_e^{ped}, the pressure pedestal is approximated by $2n_e^{ped}T_e^{ped}$ to track the dynamics. In Fig. 18, open blue symbols indicate the usual EPED1 predictions for the "final" (just prior to an ELM onset) pedestal height/width. These do change slightly with relative time because the EPED1 inputs (notably density) change a bit with relative time. This is a prediction of where the pedestal gradient should end up (and it agrees well with the later time data in both current cases). Again the error bars show standard deviations of bin averages (and the predictions vary because the inputs vary - these plots are the result of $\sim$600 EPED1 calculations each with different inputs, put into time bins). While EPED1 is normally predicting the final state, we use it to investigate the time evolution. EPED1's predicted KBM constraint scales like $(p_{ped})^{1/2}$ at a given poloidal field. Because $(p_{ped})^{1/2}$ is varying during the ELM cycle here, we can account for this variation by multiplying the EPED1 gradient by $\sqrt{(p_{ped}^{now}/p_{ped}^{final})}$, where p_{ped}^{now} is the pedestal pressure in the current time bin, and

p_{ped}^{final} is the pedestal pressure near the end of the ELM cycle. The closed blue symbols give the EPED1 KBM constraint accounting for this time variation. This represents a reasonable approximation of the KBM critical gradient at each given time bin.

Overall, EPED1 is predicting the final state well in both current cases, including a factor ~ 3 increase in gradient going from low to high current case. Figure 18(a) shows that the KBM critical gradient is quickly reached consistent with the onset of QCF indicated using a vertical line. This onset time has been determined in Fig. 13(b).In addition, the saturation of the temperature gradient coincides with EPED1 predictions of pressure gradient reaching the KBM critical gradient. Similary in the high current case, the onset of QCF and saturation of the temperature gradient are indicated using vertical lines in Fig. 18(b). EPED1 linear predictions of the dynamical evolution of the pedestal pressure gradient supports the experimental observation of the QCF onset and saturation.

Initial linear microstability properties of these edge plasmas have been analyzed for the high current case using the initial value gyrokinetic code GS2 [28]. The goal of this calculation is to explore the microinstabilities in the pedestal region. Note that extensive pedestal gyrokinetics calculations have been performed for NSTX [29] using GS2 where the basic scaling analysis is laid out for an identification of the microinstabilities in the edge. We refer the reader to Ref. [29] for details about the GS2 analysis. Given that experiment localizes the QCF in the pedestal region, which encompassed the steep gradient region and the pedestal top, GS2 calculations are performed at the pedestal top and in the top 1/2 of the steep gradient region.

Figure 19(a) indicates the pedestal top where the GS2 calculations are performed. The growth rates and frequencies are displayed in Fig. 19(b,c). Electron β scans have been performed around the nominal operating point at $\beta_e = 0.34\%$. During the scan a mode pops out when β_e reaches 0.8%, which is far from the nominal experimental β_e. The sensitivity in β_e is used to determined KBM instability, which is this case suggests that the nominal point is KBM stable.

Similarly, in Fig. 20, GS2 calculations including a scan in β_e are displayed in the top 1/2 of the steep gradient region. In this radius ($r/a = 0.985$) at the top 1/2 of the steep gradient, the nominal experimental point is near the KBM threshold. KBM instability in the steep gradient region has been reported in NSTX [29, 30] and MAST [31]. The real frequency indicates a propagation in the electron diamagnetic direction, which has been determined

using extensive parameter scans to be an hybrid TEM/KBM in Ref. [29]. This propagation direction agrees with BES estimates of the QCF propagation. Note that these local GS2 calculations are initial and that non local effects are expected to play a role in the pedestal region. Future work should employ nonlinear global calculations for a true comparison with the observed saturated QCF.

VI. SUMMARY AND DISCUSSIONS

Detailed studies of the pedestal recovery after a type I ELM and associated edge fluctuations called quasi-coherent fluctuations are presented. The inter-ELM evolution of the pedestal parameters were measured using the bunched Thomson scattering system on DIII-D. The measurements were performed for a range of plasma currents (0.7, 1.0, 1.6 MA) to show that the density gradient recovers on a much faster time scale than the temperature gradient at high current. In addition, the density gradient recovery is shown to be independent of plasma current, which potentially points to the edge recycling being responsible for the pedestal density gradient recovery. On the other hand, the temperature gradient recovery increases with the plasma current. This current dependent recovery is consistent with a longer time required for the high current case compared to the low current case to replenish and thermalize (the cold particles) the pedestal since ELM losses are larger for higher current. This does not apply to the density recovery which points to recycling being the dominant source for refilling the pedestal.

The pedestal temperature gradient recovery is found to correlate with the onset of QCF observed in density and magnetic fluctuations between ELMs. The amplitude of the QCF is observed to onset when a threshold temperature gradient is reached both in low and high current, although it is more clearly seen for the high current case since the recovery times of the density and temperature gradients are distinct. Once the QCF onsets, its amplitude tracks well the temperature gradient evolution including saturation of both amplitude and gradient prior to the next ELM. While causality in the saturated state between amplitude and gradient is difficult to show at this point, fluctuations activities correlate well with the gradient pointing to QCF playing a key role in regulating the edge transport to "halt" the temperature gradient's evolution (and linked to this evolution is the pedestal pressure gradient). Such edge regulation is speculated to occur through continuous release of energy

across the plasma boundary. The quasi-coherent fluctuations are determined to be n=-2 and n-3 toroidal modes in the low plasma current case. Unfortunately, no mode numbers analysis could be determined in the high current case due to the lack of magnetic diagnostic spectral resolution (low sampling rate of the Mirnov coils).

Furthermore, the quasi-coherent fluctuations are measured to be localized at the pedestal top of temperature using the BES but could also be localized in the pedestal within measurement uncertainties. Correlation measurements indicate that the dominant edge fluctuations, including the quasi-coherent fluctuations, are low $k_\theta \rho_s = 0.03 - 0.1$ for the low and high plasma current cases. Similar density fluctuations measurements using the DBS system detected rms density fluctuations with intermediate $k_\theta \rho_s = 0.9$. Note DBS was mostly probing the steep gradient region. The QCFs are low-k, localized in the pedestal region and propagating in the electron diamagnetic direction, onset for a given temperature gradient, and track the evolution of the temperature gradient.

EPED1 is the leading candidate in predicting the pedestal height and width. KBM physics is invoked as the limiting mechanism of the pressure pedestal gradient. Using the EPED1 model, we show good agreement of the predicted critical gradient with the onset and saturation of the QCF. The observed modes appear to onset once a gradient threshold is reached similar to where KBMs are hypothesized to occur in the EPED1 model. Note that the KBM is predicted to onset with pressure gradient. Here, we observed the QCF to onset with the temperature gradient and subsequently the QCF amplitude tracks and saturates with the temperature gradient evolution.

Several open questions remain. The most obvious one pertains to the exact nature of these fluctuations. The rather narrow radial ($\sim 1\,\mathrm{cm}$) layer in the high current case cannot exclude magnetic islands at the the pedestal top. This mode layer in low current is slightly larger ($\sim 2\,\mathrm{cm}$) and could still be associated with magnetic islands. Possible mode candidates can be reduced by examining the driving factors. While the temperature gradient appears to correlate with the amplitude evolution of the quasi-coherent fluctuations, it is worth pointing out that the mode onsets when the temperature pedestal gradient reaches a threshold. Such temperature gradient dependence cannot exclude resistive pressure-driven modes such as resistive ballooning modes. At the moment, the ballooning nature of these modes is still unclear as one would need to perform measurements at the high-field side to conclusively identify these fluctuations as of ballooning type.

Turning back to ELM and pedestal physics, it is worth noting that quasi-coherent like modes have been previously observed between ELMs on JET [21]. Similarly, Alcator, C-Mod observed such QCF between ELMs [19]. On DIII-D, BES data show that shortly after an L-H transition, coherent modes turn on [10]. At the time of turn on, the rise of ∇P_e dramatically slows. The experimental ∇P_e was shown to track the KBM ∇P_e very shortly after the transition. In JET, C-Mod, and DIII-D, the quasi-coherent fluctuations correlate with the pedestal temperature (strictly speaking with its gradient in DIII-D) increase and the density has no effect on the fluctuations' amplitude evolution. C-Mod shows that these low-k fluctuations are localized in the upper part of the steep gradient region (note the pedestal is narrow so a definite localization in the steep gradient region is not certain). On DIII-D, the QCF is also low-k and is observed to be localized at the pedestal region, which within measurement uncertainties could be the pedestal top or the steep gradient region. Initial linear microinstability analysis in the pedestal region using GS2 indicates that the top 1/2 of the steep gradient region is near the KBM threshold with propagation in the electron direction in agreement with QCF propagation as determined using BES. This begs the following questions: Are QCFs a manifestation of KBM? Thus far, based on the modeling and observations, the results suggests that QCFs are KBM. However, addressing this question more systemacally will require global nonlinear gyrokinetic calculations in the pedestal region (which has been challenging to perform) and perhaps comparison of the fluctuation spectra with these measurements. Why do QCFs precede ELMs in this case? What make QCFs different from other quasi coherent fluctuations? Indeed, the quasi-coherent nature of these fluctuations is reminiscent of EHO in the QH, QCM in EDA, and WCM on I-mode, with the main exception that all are associated with ELM-free regimes. One of these modes (QCM) has been shown to be localized in the bottom of the pedestal steep gradient using the mirror Langmuir probes on C-Mod [14]. The EHO has been shown to be saturated kink-peeling modes of low-n [32], localized in the edge pedestal region. Quasi-coherent fluctuations are observed in the region of the pedestal in the ELMy discharges discussed here and in a number of ELM-free regimes. Future work will investigate the nature of these fluctuations using nonlinear global gyro kinetic calculations (computer intensive) in the pedestal region.

VII. ACKNOWLEDGMENT

This material is based upon work supported in part by the U.S. Department of Energy, Office of Science, Office of Fusion Energy Sciences, using the DIII-D National Fusion Facility, a DOE Office of Science user facility, under Awards DE-FC02-04ER54698, DE-AC02-09CH11466, and DE-AC05-00OR22725. DIII-D data shown in this paper can be obtained in digital format by following the links at https://fusion.gat.com/global/D3D_DMP. We thank M.W. Shafer for providing the finite beam lifetime calculations. One of us (A.D.) acknowledges discussions with J.D. Callen.

[1] F. Wagner, G. Fussmann, T. Grave, M. Keilhacker, M. Kornherr, K. Lackner, K. McCormick, E. R. Müller, A Stäbler, G. Becker, K. Bernhardi, U. Ditte, . Eberhagen, O. Gehre, J. Gernhardt, G v. Gierke, E. Glock, O. Gruber, G. Haas, M. Hesse, G. Janeschitz, F. Karger, S Kissel, O. Klüber, G. Lisitano, H. M. Mayer, D. Meisel, V. Mertens, H. Murmann, W. Poschenrieder, H. Rapp, H, Röhr, F. Ryter, F. Schneider, G. Siller, P. Smeulders, F. Sóldner, E. Speth, K. H, Steuer, Z. Szymanski, and O. Vollmer, Phys. Rev. Lett **53**, 1453 (1984).

[2] J. E. Kinsey, G. M. Staebler, J. Candy, R. E. Waltz, and R. V. Budny, Nucl. Fusion **51**, 083001 (2011).

[3] P. B. Snyder, N. Aiba, M. Beurskens, R. J. Groebner, L. D. Horton, A. E. Hubbard, G. T. A. Huysmans, Y. Kamada, A. Kirk, C. Konz, A. W. Leonard, J. Lönnroth, ZC. F. Maggi, R. Maingi, T. H. Osborne, N. Ohyama, A. Pankin, S. Saarelma, G. Saibene, J. L. Terry, H. Urano and H. R. Wilson, Nucl. Fusion **49** 085035 (2009).

[4] J. R. Walk, P. B. Snyder, J. W. Hughes, J. L. Terry, A. E. Hubbard and P. E. Phillips, Nucl. Fusion **52**, 063011 (2012).

[5] R. J. Groebner, T. H. Osborne, A. W. Leonard and M. E. Fenstermacher, Nucl. Fusion **49**, 045013 (2009).

[6] J. W. Hughes P. B. Snyder, J. R. Walk, E. M. Davis, B. LaBombard, S. G. Baek, R. M. Churchill, M. Greenwald, R. J. Groebner, A. E. Hubbard, B. Lipschultz, E. S. Maqrmar, T. Osborne, M. L. Reinke, J. E. Rice, C. Theiler, J. Terry, A. E. White, D. G. Whyte, S. Wolfe and X. Q. Xu, Nucl. Fusion **53**, 043016 (2013).

[7] A. Diallo, R. Maingi, S. Kubota, A. Sontag, T. Osborne, M. Podestá, R. E. Bell, B. P. LeBlanc, J. Menard and S. Sabbagh, Nucl. Fusion **51**, 103031 (2011).

[8] A. Burckhart, E. Wolfrum, R. Fischer, K. Lackner, H. Zohm and the ASDEX Upgrade Team, Plasma Phys. Controlled Fusion **52**, 105010 (2010).

[9] A. Kirk, T. O'Gorman, S. Saarelma, R. Scannell, H. R. Wilson and the MAST Team, Plasma Phys. Controlled Fusion **51**, 065016 (2009).

[10] R. J. Groebner, C. S. Chang, J. W. Hughes, R. Maingi, P. B. Snyder, X. Q. Xu, J. A. Boedo, D. P. Boyle, J. D. Callen, J. M. Canik, I. Cziegler, E. M. Davis, A. Diallo, P. H. Diamond, J. D. Elder, D. P. Eldon, D. R. Ernst, D. P. Fulton, M. Landreman, A. W. Leonard, J. D.

Lore, T. H. Osborne, A. Y. Pankin, S. E. Parker, T. L. Rhodes, S. P. Smith, A. C. Sontag, W. M. Stacey, J. Walk, W. Wan, E. H.-J. Wang, J. G. Watkins, A. E. White, D. G. Whyte, Z. Yan, E. A. Belli, B. D. Bray, J. Candy, R. M. Churchill, T. M. Deterly, E. J. Doyle, M. E. Fenstermacher, N. M. Ferraro, A. E. Hubbard, I. Joseph, J. E. Kinsey, B. LaBombard, C. J. Lasnier, Z. Lin, B. L. Lipschultz, C. Liu, Y. Ma, G. R. McKee, D. M. Ponce, J. C. Rost, L. Schmitz, G. M. Staebler, L. E. Sugiyama, J. L. Terry, M. V. Umansky, R. E. Waltz, S. M. Wolfe, L. Zeng and S. J. Zweben, Nucl. Fusion **53**, 093024 (2013).

[11] K. H. Burrell, T. H. Osborne, P. B. Snyder, W. P. West, M. E. Fenstermacher, R. J. Groebner, P. Gohil, A. W. Leonard and W. M. Solomon, Phys. Rev. Lett. **102**, 155003 (2009).

[12] A. E. Hubbard, R. L. Boivin, R. S. Granetz, M. Greenwald, J. W. Hughes, I. H. Hutchinson, J. Irby, B. LaBombard, Y. Lin, E. S. Marmar, A. Mazurenko, D. Mossessian, E. Nelson-Melby, M. Porkolab, J. A. Snipes, J. Terry, S. Wolfe, S. Wukitch, B. A. Carreras, V. Klein and T. Sunn Pedersen, Phys. Plasmas **8**, 2033 (2001).

[13] D. G. Whyte, A. E. Hubbard, J. W. Hughes, B. Lipschultz, J. E. Rice, E. S. Marmar, M. Greenwald, I. Cziegler, A. Dominguez, T. Golfinopoulos, N. Howard, L. Lin, R. M. McDermott, M. Porkolab, M. L. Reinke, J. Terry, N. Tsujii, S. Wolfe, S. Wukitch, Y. Lin and the Alcator C-Mod Team, Nucl. Fusion **50**, 1050005 (2010).

[14] B. LaBombard, T. Golfinopoulos, J. L. Terry, D. Brunner, E. Davis, M. Greenwald, J. W. Hughes and Alcator C-Mod Team, Phys. Plasmas **21**, 056108 (2014).

[15] D. Eldon, ZB. D. Bray, T. M. Deterly, C. Liu, M. Watkins, R. J. Groebner, A. W. Leonard, T. H. Osborne, P. B. Snyder, R. L. Boivin and G. R. Tynan, Rev. Sci. Instrum. **83**, 10E343 (2012).

[16] T. H. Osborne, P. B. Snyder, K. H. Burrell, T. E. Evans, M. E. Fenstermacher, A. W. Leonard, R. A. Mpyer, M. J. Schaffer and W. P. West, J. of Physics: Conf. Series **123**, 012014 (2008).

[17] M. R. Wade, K. H. Burrell, J. T. Hogan, A. W. Leonard, T. H. Osborne, P. B. Snyder and D. Coster, Phys. Plasmas **12** , 056120 (2005).

[18] W. M. Solomon, K. H. Burrell, A. M. Garofalo, R. J. Groebner, C. J. Lasnier, M. A. Makowski, T. H. Osborne, H. Reimerdes, J. S. deGrassie, E. J. Doyle, T. E. Evans, M. E. Fenstermacher, G. L. Jackson and M. J. Schaffer, Nucl. Fusion **42**, 033007 (2012).

[19] A. Diallo, J.?W. Hughes, M. Greenwald, B. LaBombard, E. Davis, S-G. Baek, C. Theiler, P. Snyder, J. Canik, J. Walk, T. Golfinopoulos, J. Terry, M. Churchill, A. Hubbard, M. Porkolab,

L. Delgado-Aparicio, M.?L. Reinke, A. White, and Alcator C-Mod team

[20] P. Smeulders, G. D. Conway, B. Alper, B. Balet, D. V. Bartlett, D. Barba, N. Deliyanakis, T. C. Hender, and O. J. Kwon, Plasma Phys. Controlled Fusion **41**, 1303 (1999).

[21] C. P. Perez, H. R. Koslowski, T. C. Hender, P. Smeulders, A. Loarte, P. J. Lomas, G. Saibene, R. Sartori, M. Becoulet, T. Eich, R. J. Hastie, G. T. A. Huysmans, S. Jachmich, A. Rogister, F. C. Schüller and J. E. Contributors, Plasma Phys. Controlled Fusion **46**, 61 (2004).

[22] Z. Yan, G. R. McKee, R. J. Groebner, P. B. Snyder, T. H. Osborne and K. H. Burrell, Phys. Rev. Lett. **107**, 055004 (2011).

[23] Z. Yan, G. R. McKee, R. J. Groebner, P. B. Snyder, T. H. Osborne, M. N. Beurskens and K. H. Burrell, Phys. Plasmas bf 18, 056117 (2011).

[24] M. Hirsch, E. Holzhauer, J. Baldzuhn, B. Kurzan and B. Scott, Plasma Phys. Controlled Fusion **43**, 1641 (2001).

[25] E. Holzhauer, M. Hirsch, T. Grossmann, B. Brañas and F. Serra, Plasma Phys. Controlled Fusion **40**, 1869 (1998).

[26] P. B. Snyder, T. H. Osborne, K. H. Burrell, R. J. Groebner, A. W. Leonard, R. Nazikian, D. M. Orlov, O. Schmitz, M. R. Wade and H. R. Wilson, Phys. Plasmas **19**, 056115 (2012).

[27] P. B. Snyder, R. J. Groebner, A. W. Leonard, T. H. Osborne and H. R. Wilson, Phys. Plasmas **16**, 056118 (2009).

[28] Mike Kotschenreuther, G Rewoldt, and W. M. Tang, Computer Physics Communications **88**, 128 (1994).

[29] J. M. Canik, W. Guttenfelder, R. Maingi, T. H. Osborne, S. Kubota, Y. Ren, R. E. Bell, H. W. Kugel, B. P. LeBlanc and V. A. Souhkanovskii, Nucl. Fusion **53**, 113016 (2013).

[30] W. Guttenfelder, J. L. Peterson, J. Candy, S. M. Kaye, Y. Ren, R. E. Bell, G. W. Hammett, B. P. LeBlanc, D. R. Mikkelsen, W. M. Nevins and H. Yuh, Nucl. Fusion **53**, 093022 (2013).

[31] D. Dickinson, C. M. Roach, S. Saarelma, R. Scannell, A. Kirk, and H. R. Wilson, Phys. Rev. Lett. **108**, 135002 (2012).

[32] K. H. Burrell, T. H. Osborne, P. B. Snyder, W. P. West, M. E. Fenstermacher, R. J. Groebner, P. Gohil, A. W. Leonard, W. M. Solomon, Nucl. Fusion **49**, 085024 (2009).

FIG. 1: (Color online) Time history of the discharge parameters. Left panel represents the time history parameters of the low current (I_p = 0.75 MA) and the right panel those of the high current (I_p= 1.6 MA) case.

FIG. 2: (Color online) Examples of density and temperature profile evolutions during he inter-ELM phase for the high current case (I_p= 1.6 MA).

FIG. 4: (Color online) Pedestal parameter evolution relative to an ELM crash for the high current case (I_p= 1.6 MA). (a) Density pedestal height; (b) Density width; (c) Temperature pedestal height; (d) Temperature pedestal width.

FIG. 5: (Color online) The radial electric field dynamics during inter-ELM for (a) the low current case and (b) the high current case.

FIG. 6: (Color online) Pedestal gradient evolution for the low current case. Here, the gradient is computed as the ratio of height to width. Inter-ELM dynamics of (a) the density gradient and (b) the temperature gradient.

FIG. 7: (Color online) Pedestal gradient evolution for the high current case. The horizontal shaded line represents the saturation level for the low current case. The vertical lines indicate the recovery of these gradients.

FIG. 3: (Color online) Pedestal parameter evolution relative to an ELM crash for the low current case (I_p= 0.75 MA). (a) Density pedestal height; (b) Density width; (c) Temperature pedestal height; (d) Temperature pedestal width. The shaded area represents the region where recovery of these parameters occurs.

FIG. 8: (Color online) Scaling of the pedestal recovery time with plasma current for both intrinsic and triggered ELMs. Note that triggered ELMs exhibit the same pedestal characteristics as intrinsic ELMs.

FIG. 9: (Color online) Inter-ELM magnetic fluctuations spectrograms as measured using the Mirnov coils showing the QCFs in low (a) and high (b) current cases. The shaded areas on the spectrograms represent the core modes and broadband fluctuations which are not ELM related events.

FIG. 11: (Color online) BES signals $\delta I/I$ averaged over 20 kHz through 120 kHz for the low current case. (a) Radial profile of the amplitude evolution between ELMs. Here the symbols capture the time evolution. (b) Density and temperature profiles to indicate the BES measurements radial positions with measurement uncertainties as discussed in the text.

FIG. 12: (Color online) Equivalent BES localization using cross-power analysis and comparison with the magnetic spectrograms indicating that the quasi-coherent fluctuations are localized at the pedestal top.(a-c) Crosspower spectograms of poloidally separated BES channels for various radial channels. The corresponding radial points are indicated on the density and and temperature profiles (bottom left panel). The bottom right panel shows the magnetic spectrograms during the same time for guidance.

FIG. 10: (Color online) For the special case of low current case, the toroidal mode n-number analysis has been performed. Inter-ELM magnetic fluctuations n-numbers preceding the ELMs.

FIG. 13: (Color online) Fluctuations amplitude correlations with pedestal gradients' evolutions for the low current case. (a) Magnetic fluctuation spectrogram with the vertical arrows indicating the QCF frequency bands to be considered for the amplitude analysis. (b) The QCF amplitude's evolution relative to ELM for the frequency bands 23-60 kHz. Overlaid in this plot is the temperature gradient evolution indicating the onset of the QCF amplitude evolution as represented using the back arrow.

FIG. 14: (Color online) Evolution of magnetic fluctuations and pedestal gradients during ELM recovery for high current case. (a) Scaled QCF amplitude evolution for the frequency band 120-170 kHz showing the onset. Overlaid is the temperature gradient evolution. (b) The QCF amplitude is plotted against the gradient evolution to show the threshold gradient.

FIG. 15: (Color online) Inter-ELM DBS rms fluctuations for the low current case. Note that these fluctuations are measured for $k_\theta \rho_s \sim 0.9$. In addition these fluctuations are measured in the steep density gradient.

FIG. 16: (Color online) Pair-wise BES channel correlations as a function of the vertical separations of the BES views between ELMs. A correlation length of 5-6 cm was determined, which correspond to $k_\theta \rho_s \sim 0.1$. The symbols capture the time evolution of the pair-wise cross-correlation coefficients as a function of vertical/poloidal separations.

FIG. 17: (Color online) Coherency and phase shift between poloidally separated BES views for the high current case. The top panel shows the coherency between two poloidally separated BES views ($\Delta z = 5.4$ cm). The bottom panel displays the phase shifts for three poloidal separations which yield poloidal wavenumber of the QCF of $k_\theta = 0.18$-0.2 rad/cm with propagation in the electron diamagnetic direction.

FIG. 18: (Color online) EPED1 predictions for the low (a) and high current(b). The red squares represent the bin averages of DIII-D data for the pedestal pressure gradient evolution. The open blue symbols show the usual EPED1 predictions for the "final" pedestal height/width.The closed symbols give the EPED1 KBM constraint accounting for this time variation (see text for description). The vertical lines represent the time when the QCF onsets and when the temperature gradient saturates.

FIG. 19: (Color online) (a) Radial profiles of the electron temperature and density (153764 - late in the ELM cycle) indicating the GS2 analysis region at the pedestal top (b) Growth rate for multiple β_e from the nominal experiment value. (c) The associated real frequency.

FIG. 20: (color online) (a) Radial profiles of the electron temperature and density (153764 - late in the ELM cycle) indicating the GS2 analysis region at top 1/2 of the steep gradient region. (b) Growth rate for multiple β_e from the nominal experiment value. (c) The associated real frequency.

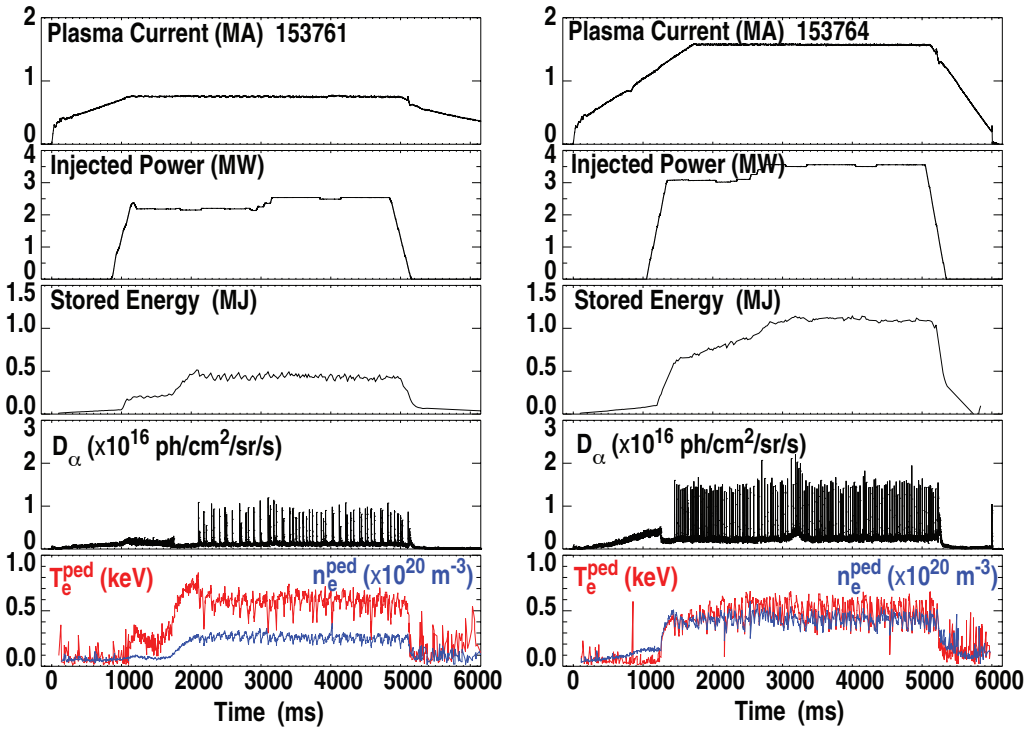

A. Diallo Figure 1

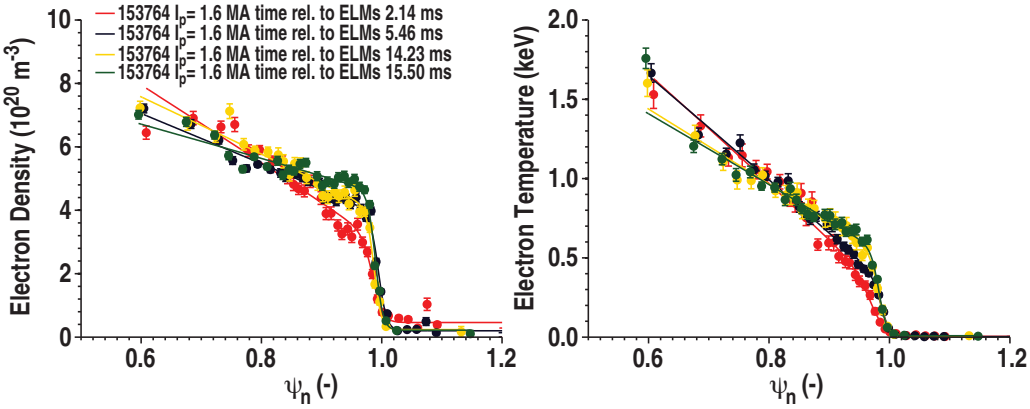

A. Diallo Figure 2

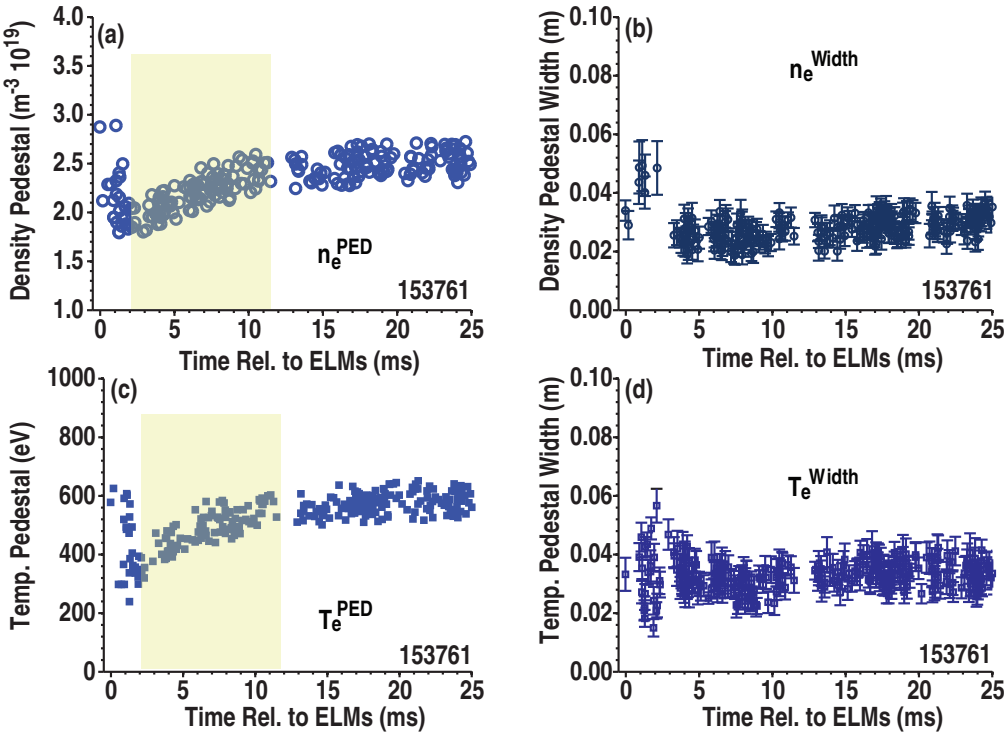

A. Diallo Figure 3

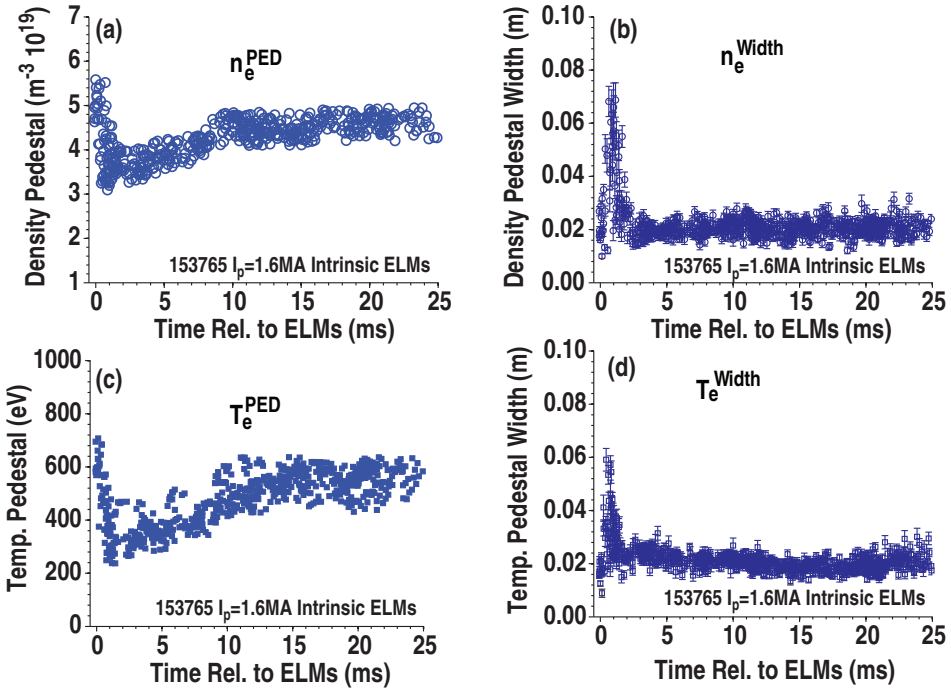

A. Diallo Figure 4

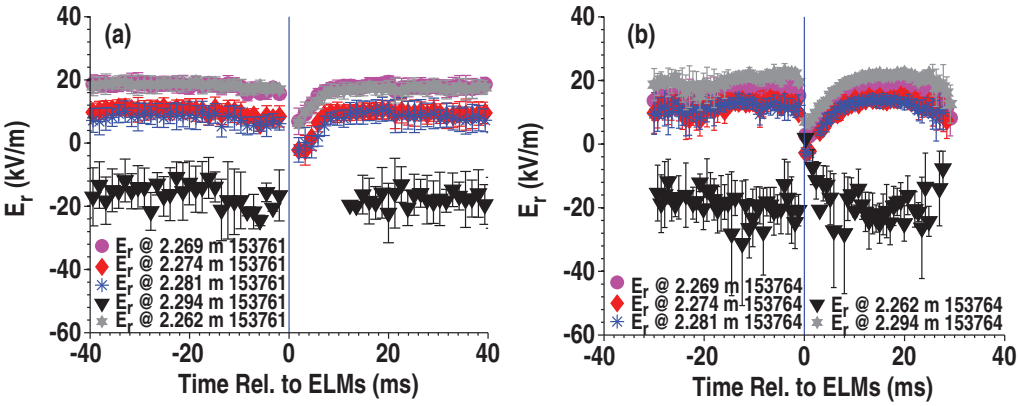

A. Diallo Figure 5

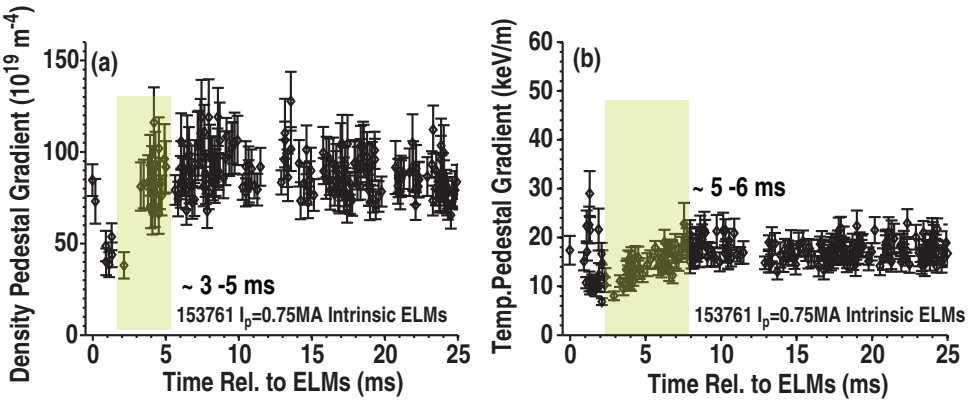

A. Diallo Figure 6

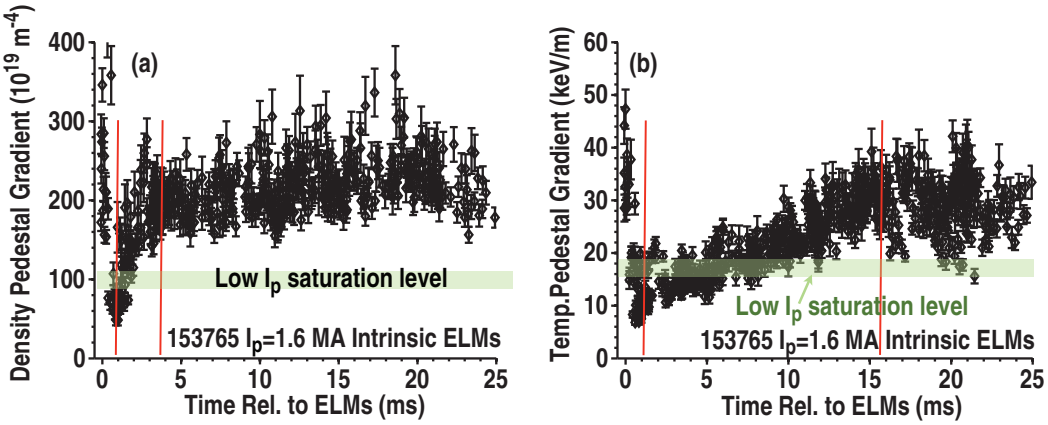

A. Diallo Figure 7

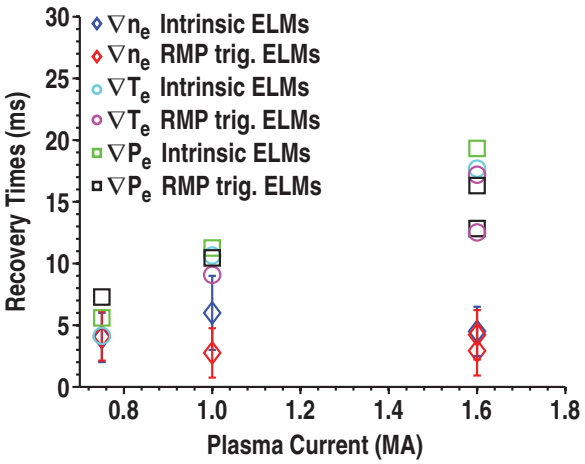

A. Diallo Figure 8

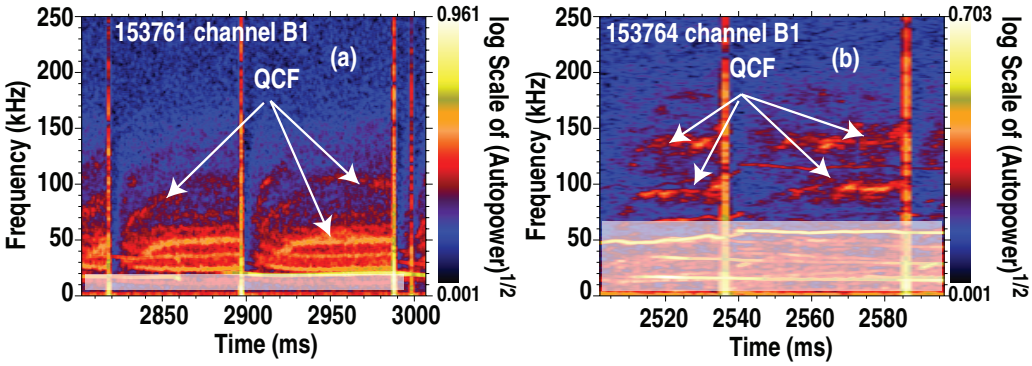

A. Diallo Figure 9

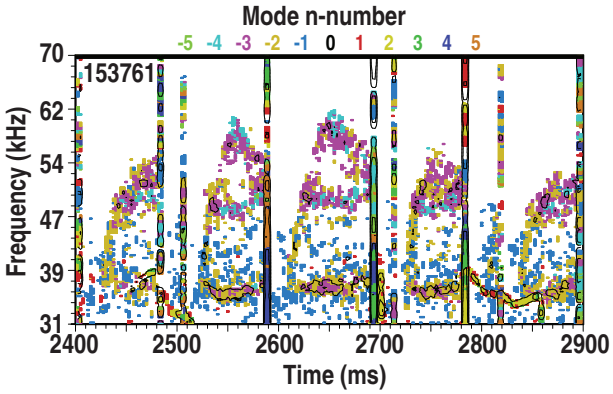

A. Diallo Figure 10

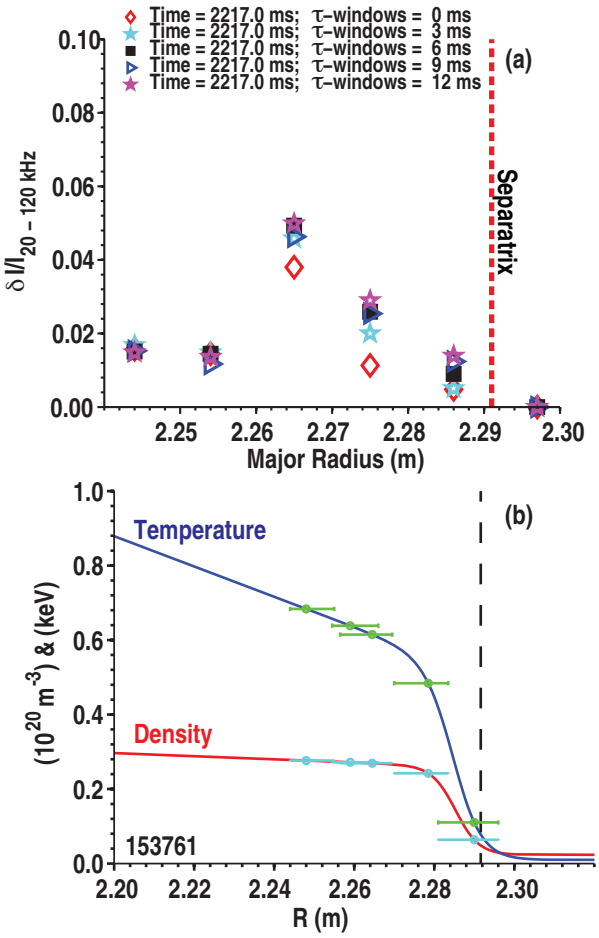

A. Diallo Figure 11

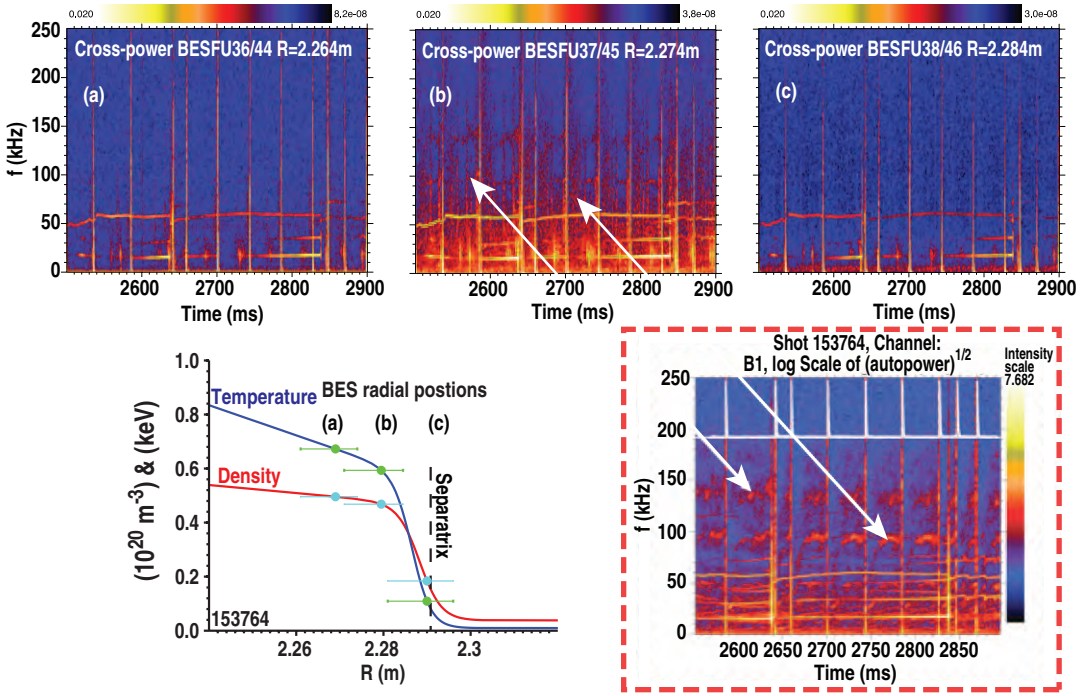

A. Diallo Figure 12

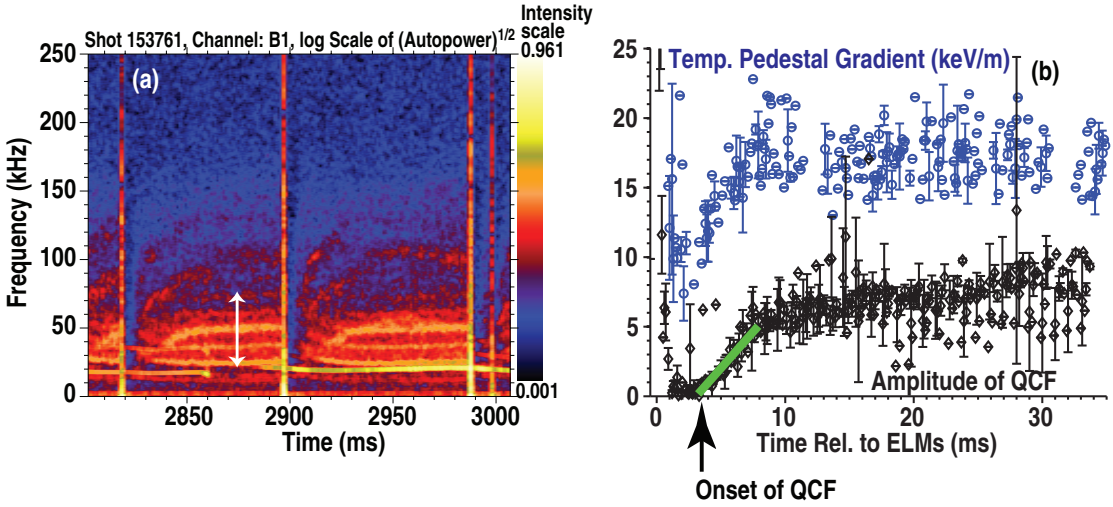

A. Diallo Figure 13

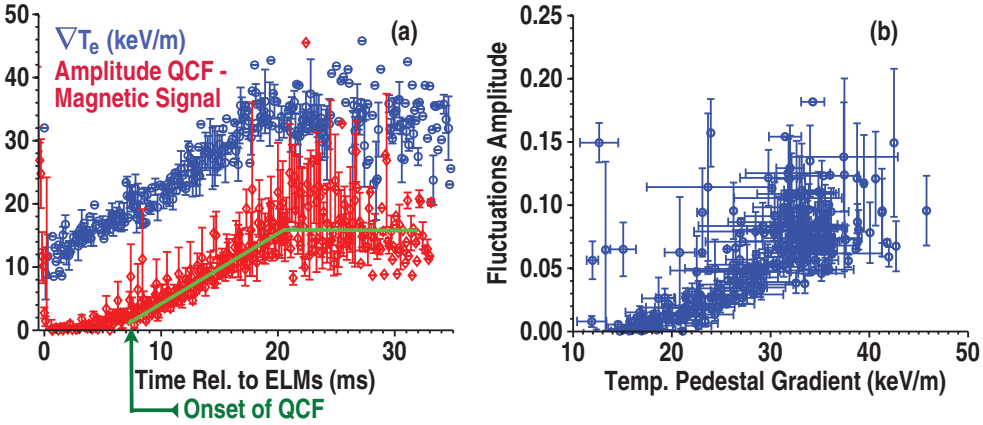

A. Diallo Figure 14

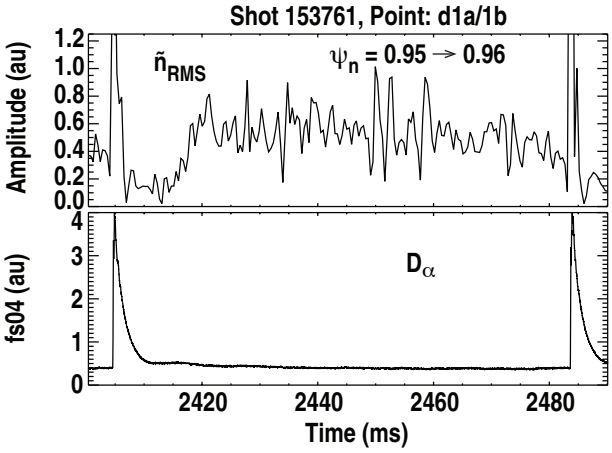

A. Diallo Figure 15

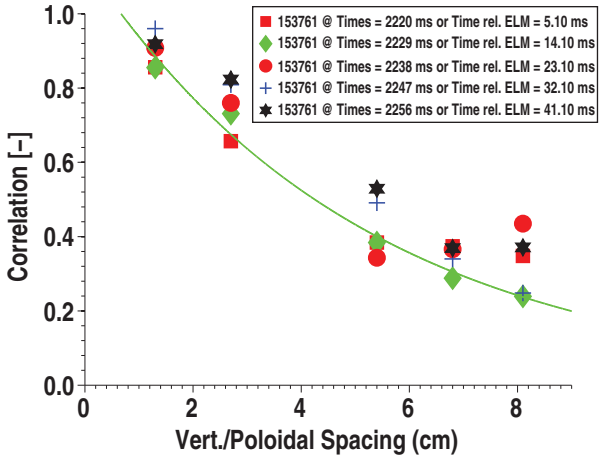

A. Diallo Figure 16

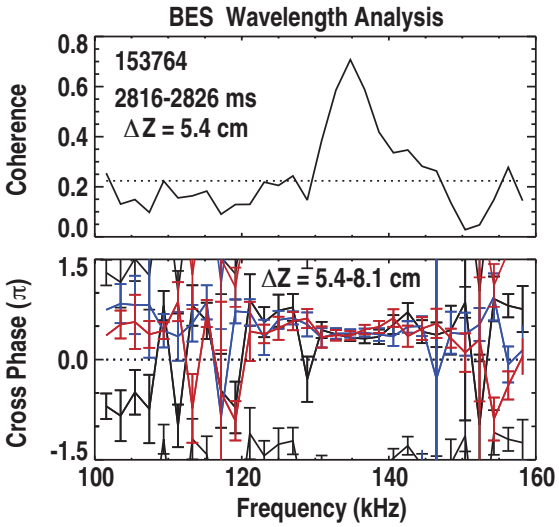

A. Diallo Figure 17

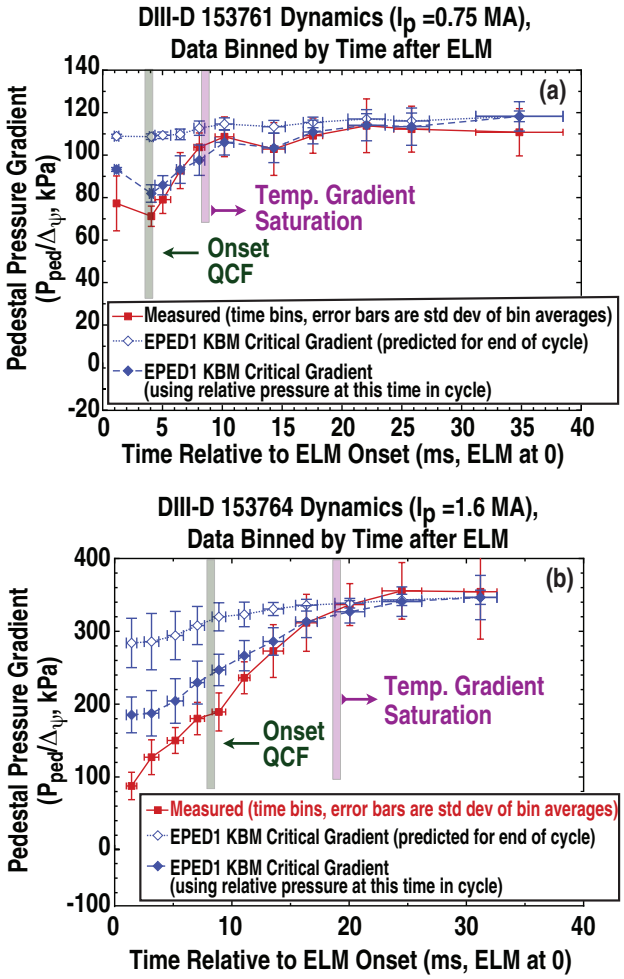

A. Diallo Figure 18

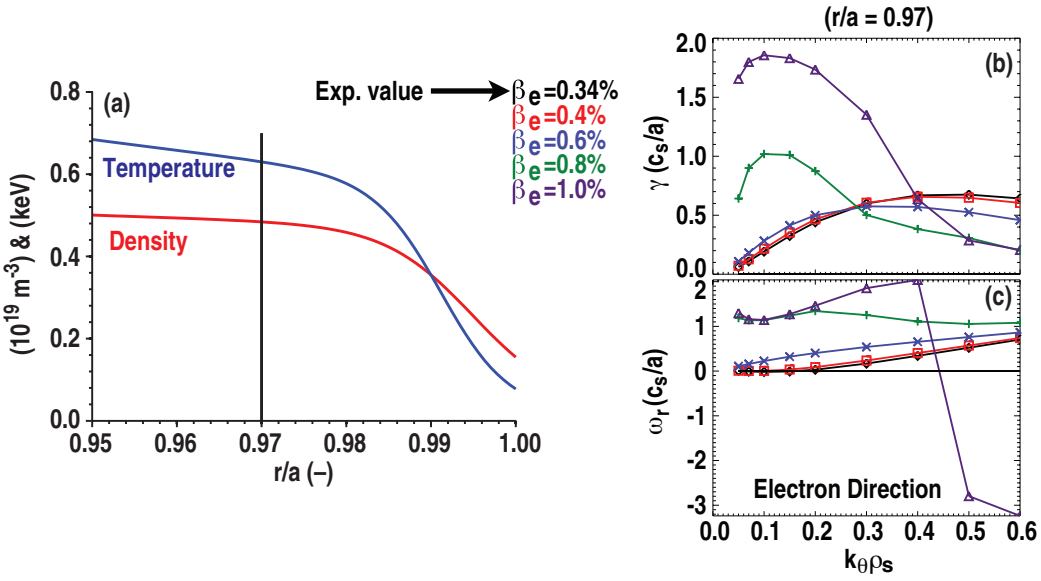

A. Diallo Figure 19

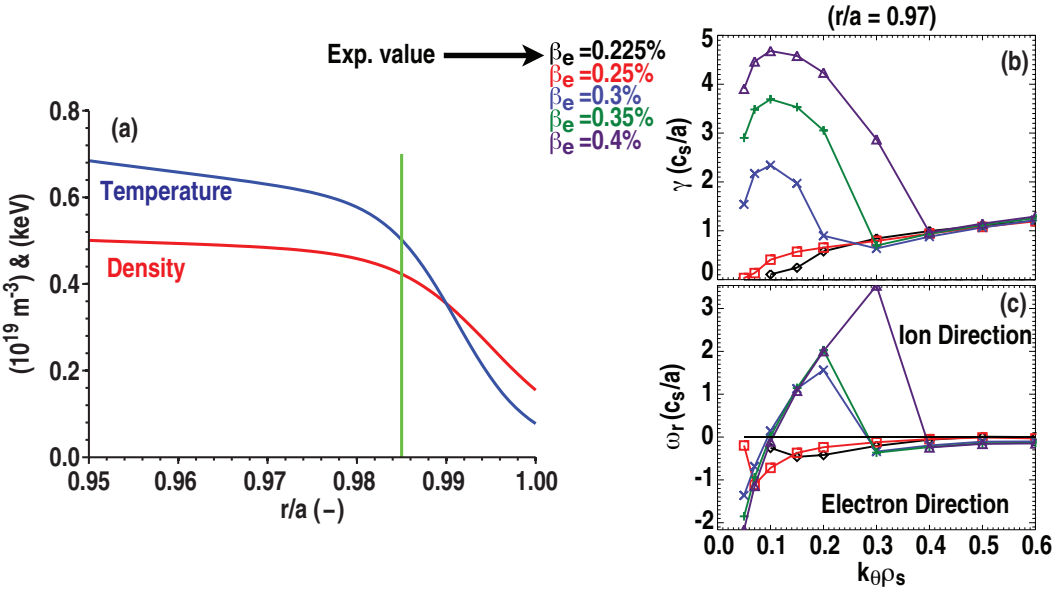

A. Diallo Figure 20

Princeton Plasma Physics Laboratory
Office of Reports and Publications

Managed by
Princeton University

under contract with the
U.S. Department of Energy
(DE-AC02-09CH11466)

P.O. Box 451, Princeton, NJ 08543
Phone: 609-243-2245
Fax: 609-243-2751

E-mail: publications@pppl.gov
Website: http://www.pppl.gov